AIChE

Particle Shape Manipulation and Optimization in Cooling Crystallization Involving Multiple Crystal Morphological Forms

Jian Wan, Xue Z. Wang, and Cai Y. Ma
Institute of Particle Science and Engineering, School of Process, Environmental and Materials Engineering,
University of Leeds, Leeds LS2 9JT, U.K.

DOI 10.1002/aic.11892

A population balance model for predicting the dynamic evolution of crystal shape distribution is further developed to simulate crystallization processes in which multiple crystal morphological forms co-exist and transitions between them can take place. The new model is applied to derive the optimal temperature and supersaturation profiles leading to the desired crystal shape distribution in cooling crystallization. Since tracking an optimum temperature or supersaturation trajectory can be easily implemented by manipulating the coolant flowrate in the reactor jacket, the proposed methodology provides a feasible closed-loop mechanism for crystal shape tailoring and control. The methodology is demonstrated by applying it to a case study of seeded cooling crystallization of potash alum. © 2009 American Institute of Chemical Engineers *AIChE J,* 55: 2049–2061, 2009

Keywords: morphological population balance model, multidimensional population balance model, crystallization control, crystal shape control and optimization

Introduction

For particulate products obtained from crystallization, crystal morphology is an important parameter because, like size distribution, it not only directly impacts the downstream processing of the particles, but also it could affect the end-use properties of the final product. Closed-loop optimization and control of crystal shape in a crystallizer, however, has long been considered to be too challenging to achieve mainly due to the limitations of available measurement techniques and modeling capabilities. However, there have been very promising advances recently in both online characterization and modeling of crystal shape evolution for crystallization processes, which could ultimately lead to practical solutions to closed-loop shape control.

For online characterization of crystal shape, recent studies on video imaging have attracted much attention, which resulted in the development of some new instrument products such as the process vision and measurement (PVM) system,[1] the particle image analyzer (PIA),[2] *in situ* particle viewer (ISPV),[3] and the online microscopy system of GlaxoSmithKline.[4–6] Several research groups across Europe, USA and Asia have explored the use of these systems for crystallization process monitoring and control. Scott et al.[7] used an inline camera prototype for qualitative monitoring of industrial crystallization. Wilkinson et al.[6] from GlaxoSmithKline were also among the first researchers to study online imaging for monitoring crystallization processes. Barrett and Glennon used the PVM imaging probe in the determination of the metastable zone of an inorganic compound.[8] Patience and Rawlings investigated the use of the PVM for measuring the shape and size information of sodium chlorate crystals.[9] Larsen et al. developed new algorithms for image analysis.[10,11] Qu et al. studied batch cooling crystallization of sulfathiazole using attenuated total reflection Fourier transform infrared (ATR-FTIR) spectroscopy and image analysis simultaneously.[12] Scholl et al.[13] studied *in situ* monitoring of polymorphic transformation using focused beam reflective measurement (FBRM), PVM, Raman and ATR-FTIR spectroscopy. Zhou et al.[14] applied

---

Correspondence concerning this article should be addressed to X. Z. Wang at x.z.wang@leeds.ac.uk.

the PVM imaging probe and developed statistical monitoring graphs using the information from image analysis. Calderon de Anda et al. have investigated the use of the GlaxoSmithKline's imaging system for monitoring the crystallization on-set and dynamic transition from one polymorph to another during crystallization of L-glutamic acid (LGA)[4]. A multiscale image analysis method[15,16] was developed and used to derive monitoring charts,[17] and then to calculate the real-time growth rates associated with the evolution of the length and width for the needle-like β-polymorphic form of LGA.[18] In addition, research is being carried out for direct three-dimensional (3-D) particle shape measurement.[5,19] Overall, all the existing investigations have demonstrated that imaging and image analysis is a very promising technique for online crystal shape characterization.

Crystal morphology prediction has been a very important research area for some time, but the focus has been on shape prediction for single crystals rather than for all the crystal population within a crystallizer. On the other hand, although population balance (PB) modeling for crystallization processes is for all crystals in a crystallizer, crystal shape was often ignored with an over-simplified crystal-size definition, i.e., the volume equivalent diameter of spheres.[20–23] Recent developments in multidimensional or morphological PB modeling, however, provide a promising technique for bridging morphology modeling at the two scales: for single crystals and for the population of crystals in a crystallizer. Puel et al.[24,25] developed a 2-D PB model to predict the growth of hydroquinone by representing the rod-like crystals with two internal coordinates, i.e., the length and width of rectangular parallelepipeds. Other crystals such as potassium dihydrogen phosphate and hen egg-white lysozyme can also be represented by two-size parameters, and thus, 2-D PB models can be developed.[26–29] By defining the size of a face as its normal distance from the geometrical center of the crystal, Ma et al.[30,31] proposed a morphological PB model that is able to simulate the dynamic size evolution in faceted directions. Shape evolution of 3-D faceted crystals involving morphological changes was also studied in the work of Zhang et al.,[32] where the entire family of possible discrete shape evolution events, such as vertices bifurcating into edges or faces were exhaustively numerated using a set of simple testable conditions. Faceted crystal shape evolution and manipulation during dissolution or growth were also studied by Snyder et al.[33,34] Zhang and Doherty[35] developed a method to combine a separate shape evolution model[36] with a standard 1-D PB model for the simultaneous prediction of crystal shape evolution and size distribution in crystallization processes of succinic acid.

Compared with the impressive progress in both online shape characterization and multidimensional (or morphological) PB modeling, research on closed-loop automatic control of crystal shape remains relatively scarce.[37] Ma et al.[27] and Lee et al.[38] presented a methodology for crystal shape control and optimization in cooling crystallization of potassium dihydrogen phosphate, which is based on optimizing the temperature profile and other influencing factors such as the seeding mass or the dissolution amount. A multidimensional PB model was developed in their work, which used two characteristic size dimensions to represent the shape of a twelve-faceted crystal. For the same chemical, Yang et al.[39] proved experimentally that the shape for a population of crystals was able to be tailored by manipulating the supersaturation profile. In addition to manipulating the temperature or supersaturation profile in cooling crystallization, another means of influencing the shape of growing crystals is the introduction of impurities. Patience and Rawlings[9] investigated the use of impurities to manipulate the shape of crystals for sodium chlorate, which also represents an important direction since the use of impurity is considered in industry as a very effective handle for shape control.

The objective of the article is two-fold. First, it is to further develop a morphological PB model for crystal shape evolution in crystallization to handle more complicated crystallization processes where multiple morphological forms co-exist, and transitions between them can take place. In addition, the new model is to be used for deriving optimal temperature and supersaturation profiles that can be tracked to obtain desired crystal shape. The rest of the article is organized as follows. The next section is devoted to the introduction of the method for representing crystal morphology using polytope geometry. The morphological PB model that can handle multiple morphological forms and model their transitions, as well as its numerical solution algorithm are then presented. Optimization of temperature and supersaturation trajectories for shape manipulation is described afterwards, which is followed by the concluding remarks.

Geometric Description of Crystal Morphology

Polytope geometry

Crystals can be viewed as convex polytopes. A convex polytope is the convex hull of a finite set of points. Convex polytopes can also be represented as the intersection of half-spaces. This intersection can be written as the following matrix inequality

$$\boldsymbol{Hx} \leq \boldsymbol{p}, \tag{1}$$

where $\boldsymbol{H}$ is an m by n matrix, $\boldsymbol{x}$ is a column vector with n components, and $\boldsymbol{p}$ is a column vector with m components. It can also be regarded as the combination of m linear constraints: $\mathbf{h}_i\boldsymbol{x} \leq p_i$, $i = 1, \ldots, m$, where $\boldsymbol{h}_i$ is the ith row of $\boldsymbol{H}$ and p_i is the i th component of $\boldsymbol{p}$. Define a vector $\boldsymbol{s}$, its ith component is denoted as s_i, then for each $i = 1, \ldots, m$, define a linear program

$$\begin{aligned} \min\ & z_i = \mathrm{s}_i \\ \text{s.t.}\quad & \boldsymbol{Hx} + \boldsymbol{s} = \boldsymbol{p} \\ & s_i \geq 0 \end{aligned} \tag{2}$$

if at optimum $z_i > 0$, then the ith constraint $\boldsymbol{h}_i\boldsymbol{x} \leq p_i$ is redundant, and it can be removed from Eq. 1 without any influence for the defined polytope.[40]

Geometric description of crystal morphology using symmetric polytopes

Crystallographic planes are usually described using a set of indices developed by the English crystallographer Miller. Miller indices (ijk) are defined as the reciprocals of the fractional intercepts, which the plane makes with the crystallographic axes. For a cubic crystal system spanned by the orthogonal unit cell axes, a crystal face with Miller indices (*ijk*) can be conveniently expressed as follows

$$\frac{i}{\sqrt{i^2+j^2+k^2}}\,x+\frac{j}{\sqrt{i^2+j^2+k^2}}\,y+\frac{k}{\sqrt{i^2+j^2+k^2}}\,z=d \tag{3}$$

where *x, y* and *z* represent the coordinates of any point satisfying Eq. 3 in the given coordinate system; $|d|$ is the perpendicular distance from the origin to the defined plane. Because most crystals are symmetric, i.e., for symmetric crystals, if the plane described by Eq. 3 is a crystal face, the following plane is also a face for the same crystal

$$\frac{i}{\sqrt{i^2+j^2+k^2}}\,x+\frac{j}{\sqrt{i^2+j^2+k^2}}\,y+\frac{k}{\sqrt{i^2+j^2+k^2}}\,z=-d \tag{4}$$

Accordingly, other symmetric faces of the crystal can also be deduced from their Miller indices. It is worthy noting that the Miller indices need further geometric transforms to obtain the corresponding polytopic planes in an orthogonal coordinate system if the crystal system is not cubic. Then a symmetric crystal can be described by the following polytope

$$\left|\begin{bmatrix}\frac{i_1}{\sqrt{i_1^2+j_1^2+k_1^2}} & \frac{j_1}{\sqrt{i_1^2+j_1^2+k_1^2}} & \frac{k_1}{\sqrt{i_1^2+j_1^2+k_1^2}}\\ \vdots & \vdots & \vdots\\ \frac{i_n}{\sqrt{i_n^2+j_n^2+k_n^2}} & \frac{j_n}{\sqrt{i_n^2+j_n^2+k_n^2}} & \frac{k_n}{\sqrt{i_n^2+j_n^2+k_n^2}}\end{bmatrix}\begin{bmatrix}x\\y\\z\end{bmatrix}\right|\le\begin{bmatrix}d_1\\ \vdots\\ d_n\end{bmatrix} \tag{5}$$

where *n* is the number of pairs of symmetric planes on the surface of the crystal with Miller index $(i_q j_q k_q)$, $q = 1, \ldots, n$, and $d_q > 0$, $q = 1, \ldots, n$ is the corresponding normal distance from the origin, as well as the crystal geometric center to one of these two symmetric planes.

Taking the crystal of potash alum ($KAl(SO_4)_2\cdot 12H_2O$) as an example, previous experimental studies found that the morphology of potash alum crystal is dominated by the octahedron (111) face, and the essentially smaller cube (100) and rhomb-dodecahedron (110) faces, with three minor faces, (221), (112) and (012) that exist only at early stages of the crystallization process and disappear quickly, hence, have not been frequently observed.[41–43] These three primary growth forms are manifested in the external morphology through the multiplicities associated with cubic symmetry which yields a total of 26 crystal growth surfaces, i.e., eight (111), six (100) and twelve (110) faces, respectively.[30] Thus, the crystal of potash alum can be described by the following symmetric polytope

$$\left|\begin{bmatrix}1/\sqrt{3} & 1/\sqrt{3} & 1/\sqrt{3}\\ 1/\sqrt{3} & 1/\sqrt{3} & -1/\sqrt{3}\\ 1/\sqrt{3} & -1/\sqrt{3} & 1/\sqrt{3}\\ 1/\sqrt{3} & -1/\sqrt{3} & -1/\sqrt{3}\\ 1 & 0 & 0\\ 0 & 1 & 0\\ 0 & 0 & 1\\ 1/\sqrt{2} & 0 & 1/\sqrt{2}\\ 1/\sqrt{2} & 0 & -1/\sqrt{2}\\ 1/\sqrt{2} & 1/\sqrt{2} & 0\\ 1/\sqrt{2} & -1/\sqrt{2} & 0\\ 0 & 1/\sqrt{2} & 1/\sqrt{2}\\ 0 & 1/\sqrt{2} & -1/\sqrt{2}\end{bmatrix}\begin{bmatrix}x\\y\\z\end{bmatrix}\right|\le\begin{bmatrix}d_1\\d_1\\d_1\\d_1\\d_2\\d_2\\d_2\\d_3\\d_3\\d_3\\d_3\\d_3\\d_3\end{bmatrix} \tag{6}$$

where d_1, d_2 and d_3 are the normal distances from the crystal geometric center to (111), (100) and (110) faces, respectively. These three faces can also be regarded as independent faces as they are geometrically independent to each other according to Eq. 6, i.e., the values of d_1, d_2 and d_3 define the shape and size of a potash alum crystal. Therefore, potash alum crystals with given d_1, d_2 and d_3 can be plotted using a polytope geometry software.[44] For example, a potash alum crystal of $d_1 = 7$ μm, $d_2 = 9$ μm, $d_3 = 8$ μm is shown in Figure 1a.

The six (100) and twelve (110) faces of a potash alum crystal can disappear if they grow too fast relative to the eight (111) faces, which results in the morphology of an octahedron.[45] Such a scenario can easily be modeled if the crystal shape is described by polytope geometry, since it is essentially the case that the constraints concerning d_2 and d_3 become redundant according to Eq. 2, and thus, they can be removed from Eq. 6. In other words, the crystal turns to be an octahedron. As an example, the crystal in Figure 1a turns to an octahedron when d_1, d_2, and d_3 grow to 8.00 μm, 14.00 μm and 10.00 μm, as depicted in Figure 1d. Figure 1 also shows a possible route for the crystal in Figure 1a to eventually transform to the shape of Figure 1d. The twelve (110) faces disappear as shown in Figure 1c when $d_1 =$ 7.75 μm, $d_2 =$ 12.00 μm and $d_3 =$ 9.50 μm, the six (100) faces disappear further as depicted in Figure 1d. This example demonstrates that polytope geometry is an effective technique for the representation of crystal shape, and for detecting morphological changes.

PB Modeling Involving Morphological Form Transitions

The term, multidimensional PB, needs clarification because in some literature it refers to PB using only one size-related dimension, i.e., the volume equivalent spherical diameter, whereas other dimensions are about other properties such as particle location, porosity, and fraction ratio. As far as this article is concerned, multidimension means multiple-size dimensions, in consistency with the literature reviewed in the Introduction. In addition, as long as causing no confusion, we will use morphological PB instead of multidimensional PB, because our approach is formulated rigorously based on the crystal morphological structure, so it can deal with complicated crystal structures of any number of facets and handle multiple morphological forms. In addition, it emphasizes reconstruction of crystal shape at any time point.

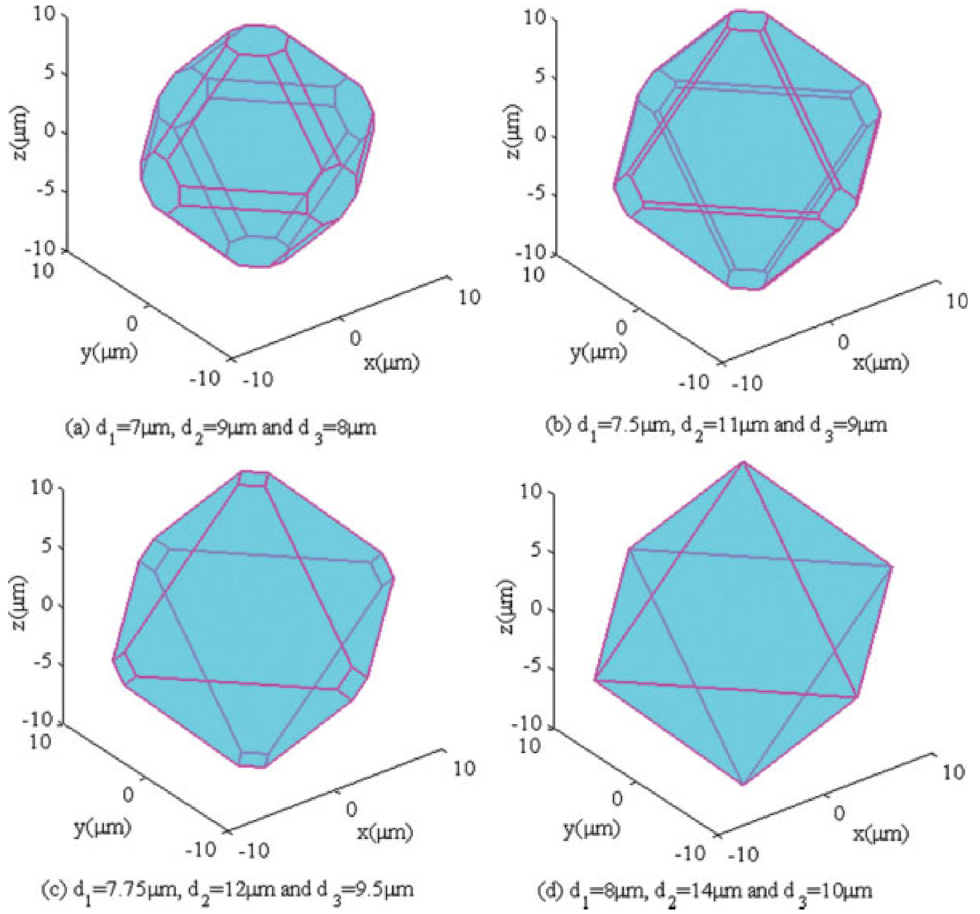
(a) d_1=7μm, d_2=9μm and d_3=8μm

(b) d_1=7.5μm, d_2=11μm and d_3=9μm

(c) d_1=7.75μm, d_2=12μm and d_3=9.5μm

(d) d_1=8μm, d_2=14μm and d_3=10μm

Figure 1. A 26 faceted potash alum crystal of (a) can grow to an eight faceted crystal shape of (d) via routes of (b) and (c).

(a) a potash alum crystal of 26 faces with its three independent sizes being $d_1 = 7.00$ μm, $d_2 = 9.00$ μm and $d_3 = 8.00$ μm; (b) 26 crystal faces with $d_1 = 7.50$ μm, $d_2 = 11.00$ μm and $d_3 = 9.00$ μm; (c) 14 crystal faces with $d_1 = 7.75$ μm, $d_2 = 12.00$ μm and $d_3 = 9.50$ μm (disappearance of 12 (110) faces), and (d) eight crystal faces with $d_1 = 8.00$ μm, $d_2 = 14.00$ μm and $d_3 = 10.00$ μm (disappearance of 12 (110) and six (100) faces). [Color figure can be viewed in the online issue, which is available at www.interscience.wiley.com.]

The generic mathematical formulation for multidimensional PB modeling, no matter employing a single-size dimension plus other external variables, or multiple-size dimensions, can be given by the following equation[30,46,47]

$$\frac{\partial\psi(\boldsymbol{x},\boldsymbol{y},t)}{\partial t}+\nabla\cdot[\psi(\boldsymbol{x},\boldsymbol{y},t)\boldsymbol{v}]+\sum_{i=1}^{n}\frac{\partial}{\partial x_i}[\psi(\boldsymbol{x},\boldsymbol{y},t)g_i(\boldsymbol{x},\boldsymbol{y},t)] = b_\psi(\boldsymbol{x},\boldsymbol{y},t)-d_\psi(\boldsymbol{x},\boldsymbol{y},t) \quad (7)$$

where $\boldsymbol{x}$ is the internal variable vector with n components, which can be parameters related to crystal size, shape, and other properties; $\boldsymbol{y}$ is the external variable vector such as spatial coordinates (y_1, y_2, y_3); ψ is the number population density function of crystals; ∇ is the gradient operator for the y coordinates. For the left side of Eq. 7, the first term is the accumulation term of ψ; the second term denotes the convection of ψ in the $\boldsymbol{y}$ space with $\boldsymbol{v}$ being the velocity vector; the third term is the convection of ψ due to particle growth in the $\boldsymbol{x}$ space with g_i being the growth rate. The first and second terms on the righthand side of Eq. 7, $b_\psi(\boldsymbol{x}, \boldsymbol{y}, t)$ and $d_\psi(\boldsymbol{x}, \boldsymbol{y}, t)$, represent the birth and death terms of ψ due to such as nucleation, aggregation and breakage. The influence of crystal positions in the crystallizer on population distributions can often be ignored for a well-mixed batch crystallizer. Furthermore, it is also reasonable to neglect the effect of agglomeration and breakage for some complex inorganic hydrate compounds such as potash alum because of their molecular and chemical properties, as argued in the literature.[30,31] Based on these assumptions, a simplified version of Eq. 7 is obtained

$$\frac{\partial\psi(\boldsymbol{x},t)}{\partial t}+\sum_{i=1}^{n}\frac{\partial}{\partial x_i}[\psi(\boldsymbol{x},t)g_i(\boldsymbol{x},t)] = b_\psi(\boldsymbol{x},t) \quad (8)$$

where $\boldsymbol{x}$ is an n-dimensional vector representing the size-related parameters of a crystal. It is usually assumed that there only exists one morphological form in the crystallizer, and thus, a single population balance equation (PBE) can describe the evolution of crystal shape and size distribution during the entire crystallization process.

In practice, however, it is not uncommon to encounter crystallization processes in which various morphological

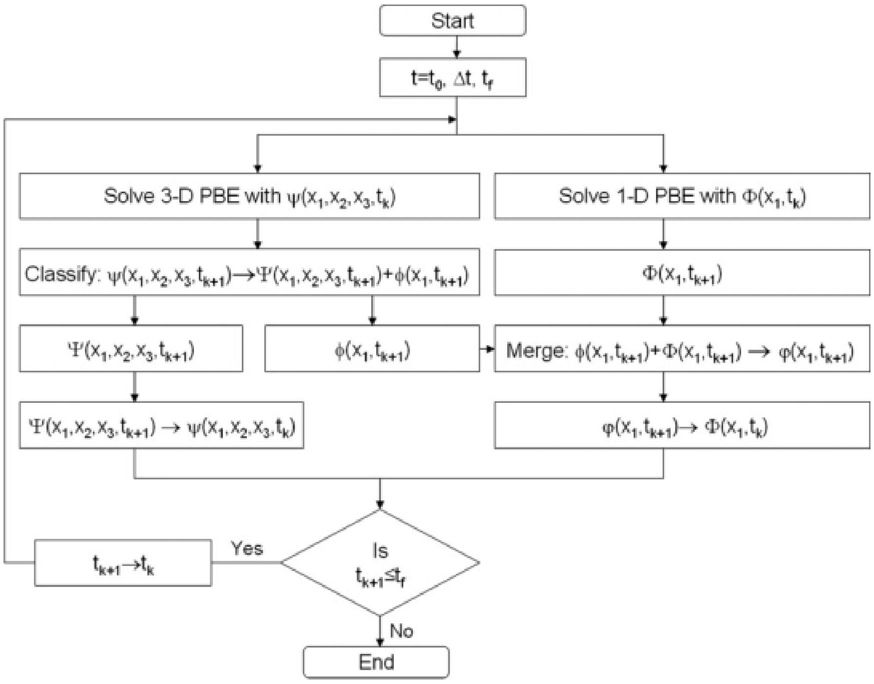

Figure 2. Morphological PB modeling involving morphological form transitions from three faceted crystals (i.e., three size dimensions) to crystals of a single-size dimension.

t_0—the initial time; Δt—sampling interval; t_f—the final simulation time; $\Psi(x_1, x_2, x_3, t_k)$—the number population density function of crystals with three faces; $\Psi(x_1, x_2, x_3, t_{k+1})$—the number population density function of crystals remaining three faces after an iteration; $\phi(x_1, t_{k+1})$—the number population density function of crystals that transformed from three faces to a single-size dimension after an iteration; $\psi(x_1, t_k)$—the number population density function of crystals with a single-size dimension; $\varphi(x_1, t_{k+1})$—the merged number population density function by combining $\phi(x_1, t_{k+1})$ and $\Psi(x_1, t_{k+1})$.

forms of crystals co-exist in the same crystallizer.[48] Furthermore, morphological changes can happen as a result of disappearance of some faces during crystal growth.[32–36,49,50] Therefore, only one PBE for modeling a single morphological form is not sufficient. Here, the morphological PB model proposed by Ma et al.[30] and Ma and Wang[31] is further developed to be able to deal with crystallization processes in which multiple morphological forms co-exist and transitions between them can take place. To introduce the approach in a simple way, consider a simple case where only two crystal morphological forms can form during cooling crystallization of a compound. One morphological form has three faces, i.e., three size dimensions x_1, x_2, and x_3, and the other has only one-size dimension x_1. At the start of the simulation, the amount of crystals for each morphological form is known, and during crystal growth, crystals that have three-size dimensions can be transformed to crystals that have only a single-size dimension. The morphological PB equations for the two types of crystals are given in Eqs. 9 and 10, respectively

$$\frac{\partial \psi(x_1,x_2,x_3,t)}{\partial t} + \sum_{i=1}^{3} \frac{\partial}{\partial x_i}[\psi(x_1,x_2,x_3,t) g_i(x_1,x_2,x_3,t)] = b_\psi(x_1,x_2,x_3,t) \quad (9)$$

$$\frac{\partial \Phi(x_1,t)}{\partial t} + \frac{\partial}{\partial x_1}[\Phi(x_1,t) g_\Phi(x_1,t)] = b_\Phi(x_1,t) \quad (10)$$

where x_1, x_2 and x_3 denote the normal distances from the crystal geometric center to these three faces, respectively; $\psi(x_1, x_2, x_3, t)$ is the number population density function of those crystals with x_1, x_2 and x_3 as their size parameters; $\Phi(x_1, t)$ is the number population density function of those crystals with x_1 as their size parameter, i.e., those crystals that have only one size dimension; g_1, g_2 and g_3 are the corresponding growth rates in x_1, x_2 and x_3 directions, respectively; $g_\Phi = g_1$ is the growth rate in x_1 direction; $b_\psi(x_1, x_2, x_3, t)$ and $b_\Phi(x_1, t)$ are the corresponding birth terms. For this simple scenario, the method for carrying out morphological PB is shown in Figure 2. At any given time step $t = t_k$, with the known number population density functions $\psi(x_1, x_2, x_3, t_k)$ and $\Phi(x_1, t_k)$ for the two morphological forms, Eqs. 9 and 10 are solved simultaneously. Then the solution $\psi(x_1, x_2, x_3, t_{k+1})$ is split into $\Psi(x_1, x_2, x_3, t_{k+1})$ and $\phi(x_1, t_{k+1})$, the later accounts for crystals that have transformed from three-size dimensions to only one-size dimension, whereas the former represents those that have not experienced such a transition, therefore, remaining three-size dimensions. $\phi(x_1, t_{k+1})$ is to be merged with $\Phi(x_1, t_{k+1})$ as they all belong to the same morphological form of a single-size dimension. Thus, updated number population density functions for these two morphological forms are passed onto Eqs. 9 and 10 for the next iteration. It is worthy noting that mass balance is also applied to update the supersaturation in the crystallizer at each time step based on the updated number population density functions. The case described before is simple, but the principle is clearly applicable to much more complicated situations such as the multiple morphological forms in Figures 1. The resulting multiple population balance equations of various dimensionalities are to be solved simultaneously at each time step.

Numerical Solution Algorithm

Various numerical algorithms for solving PB equations have been studied in the literature, such as moment of classes, method of characteristics, method of lines, generalized finite-element scheme, moving grid technique, hierarchical solution strategy based on multilevel discretization, and the cell-ensemble method. Based on the literature review of these algorithms,[28] and our previous experience on the use of moment of classes,[30] high-resolution algorithm is chosen in this study.

High-resolution algorithms were developed initially in computational physics for numerical solution of hyperbolic partial differential equations.[51] The standard high-resolution algorithms are directly applicable to homogeneous 1-D partial differential equations.[28] Using a technique called dimensional splitting, multidimensional partial differential equations can be decomposed into multiple 1-D problems, and thus, the standard high-resolution algorithms can be applied to solve them sequentially.[27] The nonhomogeneous terms usually encountered in PB equations can also be added to the distribution function at each time step using Godunov splitting.[27,28] Although high-resolution algorithms were applied in the literature only to monosize dimensional and 2-D PB equations,[26–28] it can be adapted to solve the current problem of three or more size dimensional PB equations, as illustrated later.

Considering the homogeneous 1-D PBE with size-independent growth

$$\frac{\partial \Phi(x_1,t)}{\partial t} + g_1 \frac{\partial \Phi(x_1,t)}{\partial x_1} = 0 \tag{11}$$

where $\Phi(x_1, t)$ is the number population density function and the growth rate $g_1 > 0$. A class of high-resolution finite volume algorithms with approximate second-order accuracy has the following form[28]

$$\begin{aligned}\Phi_e(x_1,t_{k+1}) = {} & \Phi_e(x_1,t_k) - \frac{\xi g_1}{h}(\Phi_e(x_1,t_k) - \Phi_{e-1}(x_1,t_k)) \\ & - \frac{\xi g_1}{2h}\left(1 - \frac{\xi g_1}{h}\right) \times [(\Phi_{e+1}(x_1,t_k) - \Phi_e(x_1,t_k))\eta_e \\ & - (\Phi_e(x_1,t_k) - \Phi_{e-1}(x_1,t_k))\eta_{e-1}]\end{aligned} \tag{12}$$

where ξ and h denote the time and size intervals, respectively; k and e are the corresponding integers to mark the time space and the size space, respectively. The flux-limiter function $\eta_e = \eta(\theta_e)$ depends on the degree of smoothness of the distribution, which is further quantified by the ratio of two consecutive gradients

$$\theta_e = \frac{\Phi_e(x_1,t_k) - \Phi_{e-1}(x_1,t_k) + \varepsilon}{\Phi_{e+1}(x_1,t_k) - \Phi_e(x_1,t_k) + \varepsilon} \tag{13}$$

where ε is a small value added to avoid division by zero, e.g., $\varepsilon = 10^{-10}$ just as in the work of Qamar et al.[52] Many flux-limiter functions have been proposed, and each flux limiter leads to a different high-resolution method. A commonly-used flux limiter called the Van Leer flux limiter is given as follows[28]

$$\eta(\theta_e) = \frac{|\theta_e| + \theta_e}{1 + |\theta_e|} \tag{14}$$

Consider the homogeneous 3-D PBE with size-independent growth as well

$$\frac{\partial \psi(x_1,x_2,x_3,t)}{\partial t} + \sum_{i=1}^{3} \frac{g_i \partial\{\psi(x_1,x_2,x_3,t)\}}{\partial x_i} = 0 \tag{15}$$

where x_1, x_2 and x_3 are the lengths on three independent directions, while g_1, g_2 and g_3 are their corresponding growth rates. At time instant t_{k-1}, Eq. 15 becomes

$$\frac{\partial \psi}{\partial t} + g_1 \frac{\partial \psi}{\partial x_1} + g_2 \frac{\partial \psi}{\partial x_2} + g_3 \frac{\partial \psi}{\partial x_3} = 0 \tag{16}$$

with the initial crystal-size distribution $\psi(x_1, x_2, x_3, t_{k-1})$.

The analytical solution to this specific partial differential equation at t_k is as follows

$$\begin{aligned}\psi(x_1,x_2,x_3,t_k) = {} & \psi(x_1 - g_1(t_k - t_{k-1}),\ x_2 \\ & - g_2(t_k - t_{k-1}), x_3 - g_3(t_k - t_{k-1}), t_{k-1})\end{aligned} \tag{17}$$

The same partial differential equation can be solved in three steps using dimensional splitting. Concretely, for the first 1-D partial differential equation

$$\frac{\partial \hat{\psi}}{\partial t} + g_1 \frac{\partial \hat{\psi}}{\partial x_1} = 0 \tag{18}$$

with the initial condition $\psi(x_1, x_2, x_3, t_{k-1})$, its solution is as follows

$$\hat{\psi}(x_1,x_2,x_3,t_k) = \psi(x_1 - g_1(t_k - t_{k-1}), x_2, x_3, t_{k-1}). \tag{19}$$

Now using $\hat{\psi}(x_1, x_2, x_3, t_k)$ as the initial condition to solve the second partial differential equation

$$\frac{\partial \tilde{\psi}}{\partial t} + g_2 \frac{\partial \tilde{\psi}}{\partial x_2} = 0 \tag{20}$$

with the renewed initial condition at $\hat{\psi}(x_1, x_2, x_3, t_k)$ at $\mathrm{t} = \mathrm{t}_{\mathrm{k}}-1$. The solution to the second partial differential equation at t_k is as follows

$$\begin{aligned}\tilde{\psi}(x_1,x_2,x_3,t_k) & = \hat{\psi}(x_1, x_2 - g_2(t_k - t_{k-1}), x_3, t_k) \\ & = \psi(x_1 - g_1(t_k - t_{k-1}), x_2 - g_2(t_k - t_{k-1}), x_3, t_{k-1})\end{aligned} \tag{21}$$

Now using $\tilde{\psi}(x_1, x_2, x_3, t_k)$ as the initial condition to solve the third partial differential equation

$$\frac{\partial\tilde{\psi}}{\partial t} + g_3\frac{\partial\tilde{\psi}}{\partial x_3} = 0 \qquad (22)$$

with the renewed initial condition at $\hat{\psi}(x_1, x_2, x_3, t_k)$ at $t = t_{k-1}$. The solution to the third partial differential equation at t_k is identical to the analytical solution Eq. 17

$$\begin{aligned}\tilde{\psi}(x_1,x_2,x_3,t_k) &= \tilde{\psi}(x_1,x_2,x_3 - g_3(t_k - t_{k-1}),t_k)\\ &= \psi(x_1 - g_1(t_k - t_{k-1}),x_2 - g_2(t_k - t_{k-1}),\\ &\qquad x_3 - g_3(t_k - t_{k-1}),t_{k-1})\end{aligned} \qquad (23)$$

As demonstrated previously, the 3-D partial differential equation can be split into three 1-D partial differential equations according to x_1, x_2 and x_3, which can then be solved sequentially at each time step using the high-resolution algorithms.

Optimization of Temperature and Supersaturation Trajectories

Since the morphological PB model describes the dynamic evolution of particle shape as well as particle-size distribution for all crystals in the crystallizer as a function of the operational conditions, i.e., supersaturation or reactor temperature, it can be used to derive an optimal supersaturation or temperature profile, which can lead to desired particle shape and size distribution. This provides a feasible mechanism for crystal shape control that can be easily implemented because an optimal temperature or supersaturation profile can be tracked by a simple feedback or a cascade control system through manipulating the coolant flowrate in the reactor jacket.

This section demonstrates the process of obtaining the optimal temperature and supersaturation profiles for a defined objective function related to the shape of crystals of potash alum. For the potash alum crystal that has 26 faces, it can be modeled as having three independent faces (111), (100) and (110), as have been handled in the literature,[30,31] where x_1, x_2, and x_3 denote the corresponding normal distances from the origin, as well as the crystal geometric center to these three independent faces. Suppose the desired shape for the crystals are

$$x_1/x_2 = a_1, x_2/x_3 = a_2 \qquad (24)$$

where a_1 and a_2 are the desired aspect ratios between x_1 and x_2, x_2 and x_3, respectively.

Then the optimization problem can be formulated as

$$\min_{r(t)} \sum_{x_1,x_2,x_3} (\psi(x_1,x_2,x_3,t_f)[(x_1/x_2 - a_1)^2 + (x_2/x_3 - a_2)^2])/ \sum_{x_1,x_2,x_3} \psi(x_1,x_2,x_3,t_f) \qquad (25)$$

subject to

$$r_L \le r(t) \le r_U \qquad (26)$$

where $r(t)$ is the cooling rate with the lower bound r_L and the upper bound r_U; $\sum_{x_1,x_2,x_3} \psi(x_1, x_2, x_3, t_f)$ corresponds to the sum of all number population densities at $t = t_f$ across the discrete grid of the whole parameter space; and $\psi(x_1, x_2, x_3, t_f)$ is the predicted final number population density function using the new morphological PB model. It needs to point out that the objective function defined by Eq. 25 only considers the crystals with 26 faces, i.e., crystal shape represented by Figure 1a. Apparently, there are many other ways to define objective functions concerning particle shape, size distributions and all the morphological forms. Here we use Eq. 25 purely for the purpose of demonstrating the principle that for a given objective function, optimal temperature and supersaturation profiles can be obtained using the morphological PB model presented in this article. Furthermore, except for the imposed constraint on cooling rates, state constraints for specifying the crystal shape and size distribution can also be imposed to formulate a typical model predictive control scheme, as pointed out in the work of Shi et al.[29,53]

The growth rates of the (111), the (100) and the (110) faces are[31]

$$g_1 = 7.753 \times 10^{-7}\sigma_{\text{eff}_1}^{1.5} \qquad (27)$$

$$g_2 = 1.744 \times 10^{-6}\sigma_{\text{eff}_2}^{1.5} \qquad (28)$$

$$g_3 = 1.124 \times 10^{-6}\sigma_{\text{eff}_3}^{1.5} \qquad (29)$$

where σ_{eff_1}, σ_{eff_2} and σ_{eff_3} are the corresponding effective relative supersaturation, which is a function of the temperature T(K), crystal size, and the relative supersaturation $\sigma = c/c^* - 1$ with c, the solution concentration, being defined as the molar weight per volume of solution in a reactor, and c^*, the solubility of potash alum. Solubility is estimated using Eq. 30[54]

$$\ln(c^*) = 12.1/\mathrm{T} + 10.47\ln(\mathrm{T}) - 65.73. \qquad (30)$$

In the simulation, it was assumed that there are initially 4843355 potash alum crystals all with 26 faces in a 500 mL reactor, the corresponding number population density function $\psi(\mathrm{x}_1, \mathrm{x}_2, \mathrm{x}_3, \mathrm{t}_0)$ for these potash alum crystals with eight (111), six (100) and 12 (110) faces is shown in Figure 3. It was also assumed that the initial temperature in the reactor is 38°C, and the initial relative supersaturation is 0.06589. As discussed earlier, one or two of the three faces (111), (100) and (110) may disappear during growth, and thus, theoretically there exist seven possible morphological forms in the reactor,[55,56] as depicted in Figure 4. As a result, seven number population density functions are needed: $\psi(x_1, x_2, x_3, t)$ for those crystals with 26 faces; $\Gamma_{201}(x_1, x_2, t)$ for crystals with eight (111) and six (100) faces, $\Gamma_{202}(x_1, x_3, t)$ for crystals with eight (111) and twelve (110) faces; $\Gamma_{203}(x_2, x_3, t)$ for crystals with six (100) and twelve (110) faces; $\Phi_{101}(x_1, t)$ for crystals with eight (111) faces; $\Phi_{102}(x_2, t)$ for crystals with six (100) faces; and $\Phi_{103}(x_3, t)$ for those with twelve (110) faces. Accordingly, seven morphological PB equations are formulated and solved simultaneously. At each time step, the number population density function for every morphological form is updated, considering the possible transitions

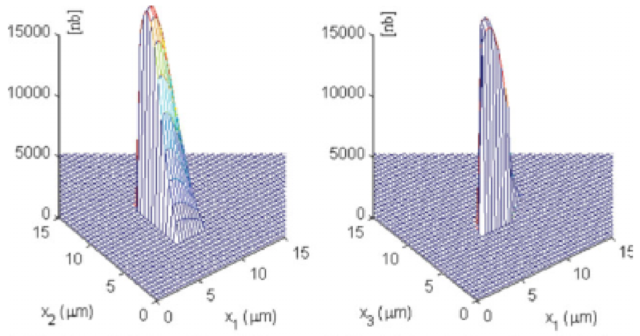

(a) The initial distribution with x_3=8.06 μm (b) The initial distribution with x_2=10.175 μm

Figure 3. The initial number population density functions of crystals with 26 faces: (a) at fixed value for x_3 = 8.06 μm, and (b) at fixed value for x_2 = 10.175 μm.

[Color figure can be viewed in the online issue, which is available at www.interscience.wiley.com.]

from one morphological form to another. In fact, for crystals with 26 faces, 14 faces and 20 faces, they all can transform to crystals having eight faces. The crystal size ranges in x_1, x_2 and x_3 directions are between 0 to 43.2 μm, 0 to 64 μm and 0 to 60 μm, respectively. The number of the size classes is 118 × 116 × 116, and the corresponding width is 0.36 × 0.55 × 0.52 μm.

Optimization is performed using Eq. 25 as the objective function and setting $a_1 = a_2 = 1$. The optimal temperature profile shown in Figure 5 is obtained when the value of the objective function for Eq. 25 reached 0.0521. In Figure 5, the lower bound and the upper bound of the cooling rate are $r_L = 0.02$°C/min and $r_U = 0.3$°C/min, respectively. The supersaturation trajectory corresponding to the optimal temperature profile is shown in Figure 6. As depicted in Figure 7, the percentages of number of crystals for the seven morphological forms change with time as a result of transitions between them. At the start of the simulation, all crystals, i.e., 100%, are crystals of 26 faces as in Figure 7a, and all other morphological forms account for 0%. By the end of the simulation, 70% crystals remain to have 26 faces. Figure 7 also shows that for some morphological forms the number percentages increase linearly, e.g., for crystals of eight and twelve faces as shown in Figures 7e and 7g, respectively, but for some other morphological forms, e.g., crystals with 14 faces in Figure 7b, the number increases initially then decreases. It is also noticed that crystals of 26 faces still dominate in terms of the percentage of crystal numbers despite the morphological transitions.

Figure 8 plots the number population density function $\psi(x_1, x_2, x_3, t)$ at four instants for crystals with 26 faces with the fixed $x_3 = 8.06$ μm. As expected, the plot also shows a downward trend with time in terms of number of crystals, which is due to transition to other morphological forms as explained earlier. Figure 9 shows the shape of typical 26 faceted crystals at different instants. Please note that the crystals in Figure 9 are not the same crystal at different times of growth: each is an example of crystals for the specified moment that the size at each face direction is the mean value for all the crystals of the same morphological form. Figure 10 demonstrates the shape evolutions of the same crystal that initially has 26 faces as shown in Figure 10a and remains to have 26 faces at the end of the simulation, but the shape and size in every face direction are changed as

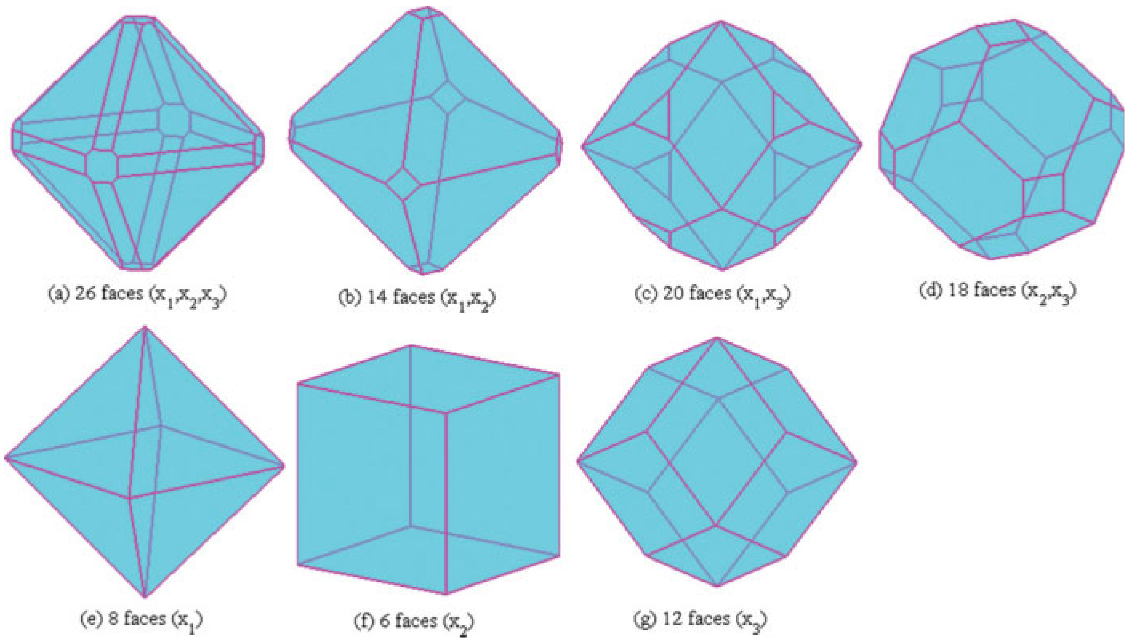

(a) 26 faces (x_1,x_2,x_3) (b) 14 faces (x_1,x_2) (c) 20 faces (x_1,x_3) (d) 18 faces (x_2,x_3)

(e) 8 faces (x_1) (f) 6 faces (x_2) (g) 12 faces (x_3)

Figure 4. A 26 faceted potash alum crystal (a) can possibly grow to another six morphological forms.

(a) a crystal with eight (111), six (100) and twelve (110) faces; (b) crystal with eight (111) and six (100) faces; (c) crystal with eight (111) and twelve (110) faces; (d) crystal with six (100) and twelve (110) faces; (e) crystal with eight (111) faces; (f) crystal with six (100) faces, and (g) crystal with twelve (110) faces. [Color figure can be viewed in the online issue, which is available at www.interscience.wiley.com.]

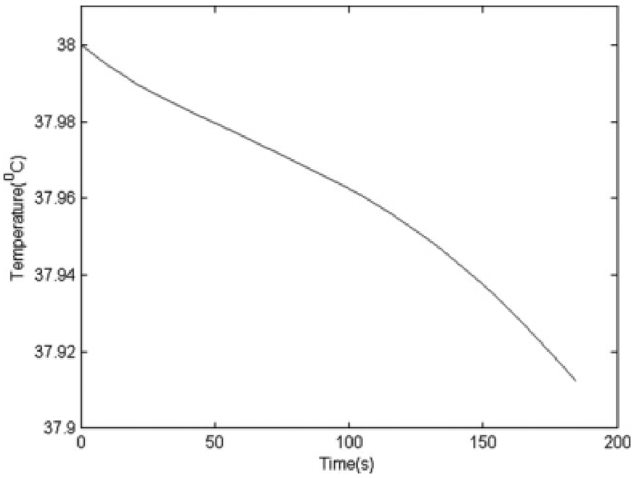

Figure 5. The optimal temperature profile.

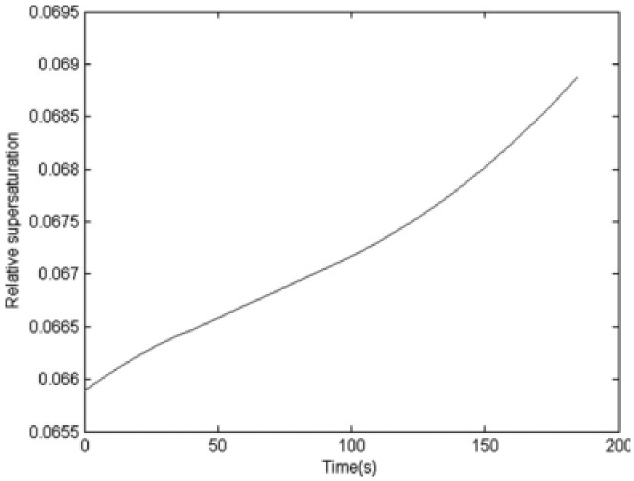

Figure 6. The optimal supersaturation profile.

seen in Figure 10e. In Figure 10e, the outer wire-framed polytope shows the desired shape. The initial shape of this crystal is typical of those crystals representing the maximal number density in the reactor. Its sizes at $t = 0$ in the three independent face directions are $x_1 = 7.020$ μm, $x_2 = 10.175$ μm and $x_3 = 8.060$ μm. As an indication of the shape change as a result of optimization, Figure 11 plots the change of $(x_1/x_2 - 1)^2 + (x_2/x_3 - 1)^2$ for the single crystal shown in Figure 10. It can be seen that its morphology does grow to approach the desired morphology, i.e., $(x_1/x_2 - 1)^2 + (x_2/x_3 - 1)^2$ approaches zero as the operating condition follows the optimal supersaturation profile.

Concluding Remarks

The presented new morphological PB model has proved to be able to simulate cooling crystallization processes where

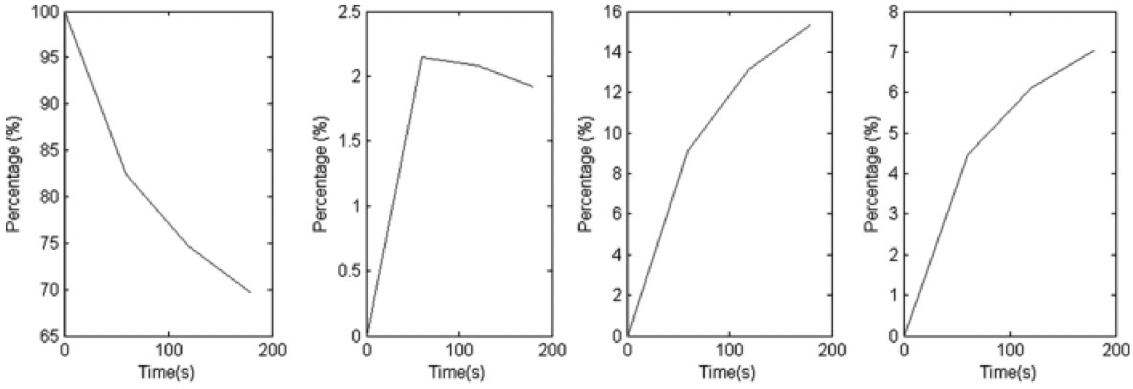

(a) Crystals with 26 faces

(b) Crystals with 14 faces

(c) Crystals with 20 faces

(d) Crystals with 18 faces

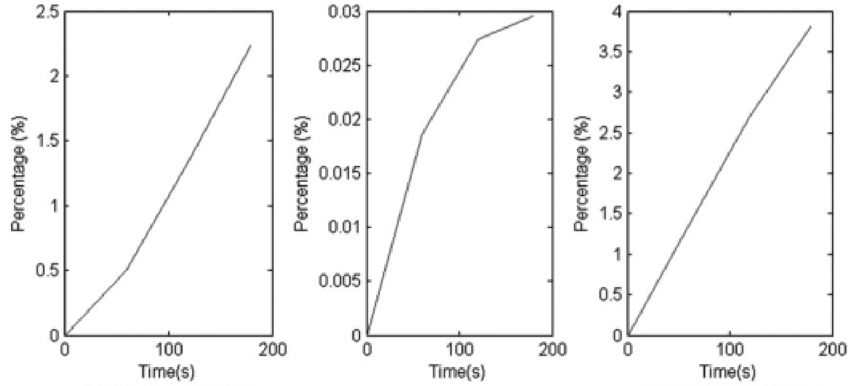

(e) Crystals with 8 faces

(f) Crystals with 6 faces

(g) Crystals with 12 faces

Figure 7. Change with time of the percentage of the number of crystal for each of the seven morphological forms.

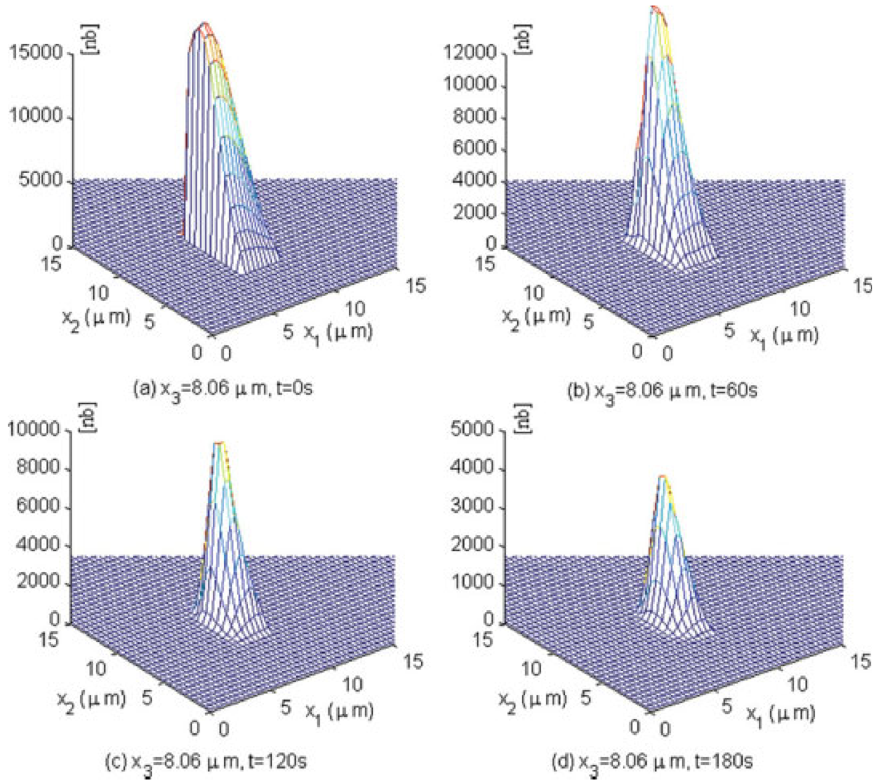

(a) x_3=8.06 μm, t=0s

(b) x_3=8.06 μm, t=60s

(c) x_3=8.06 μm, t=120s

(d) x_3=8.06 μm, t=180s

Figure 8. The number density functions at four different instants for crystals with 26 faces, but three independent size dimensions x_1, x_2, and x_3, showing a downward trend with time in number of crystals.

The function is plotted for a fixed value for one size dimension $x_3 = 8.06$ μm. [Color figure can be viewed in the online issue, which is available at www.interscience.wiley.com.]

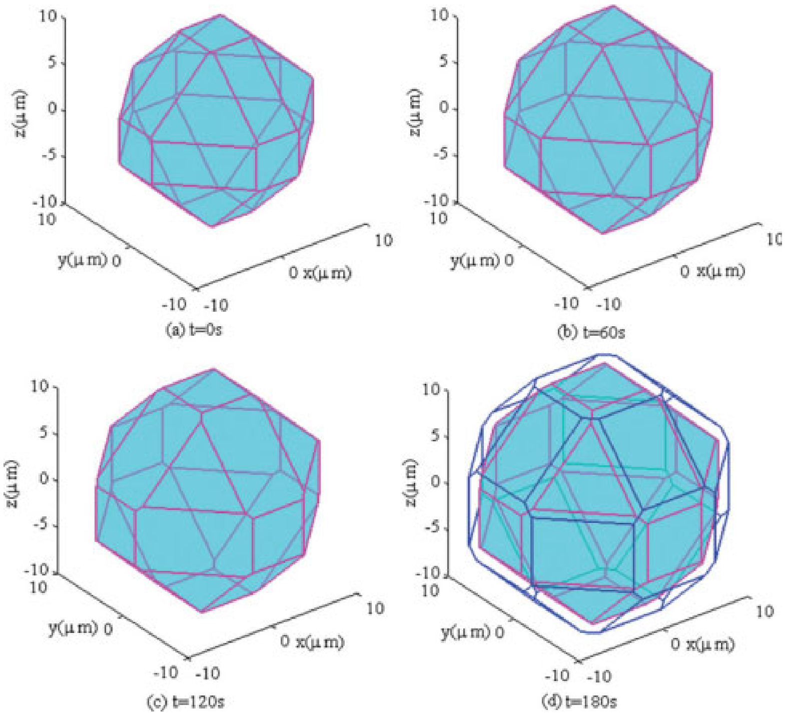

(a) t=0s

(b) t=60s

(c) t=120s

(d) t=180s

Figure 9. Typical crystals that the size in every face direction is the mean size of crystals at that specified time (The outer wire-framed polytope in (d) is the desired crystal shape).

[Color figure can be viewed in the online issue, which is available at www.interscience.wiley.com.]

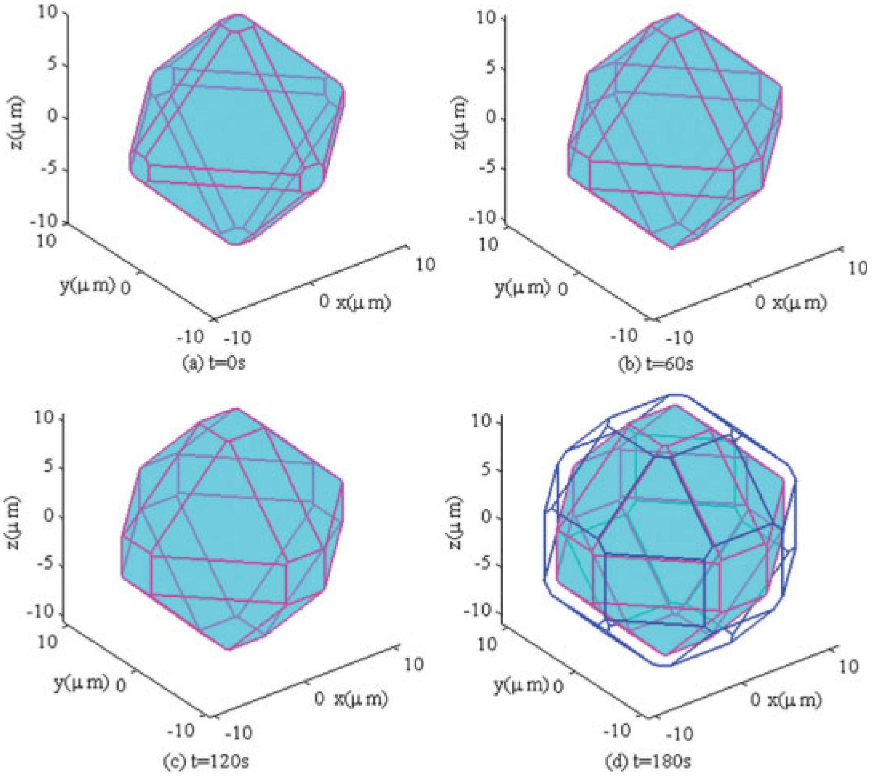

(a) t=0s

(b) t=60s

(c) t=120s

(d) t=180s

Figure 10. The shape evolution of a crystal under the optimal supersaturation trajectory (The outer wire-framed polytope in (d) is the desired crystal shape).

[Color figure can be viewed in the online issue, which is available at www.interscience.wiley.com.]

multiple morphological forms co-exist in the crystallizer and transitions between them can happen. It also demonstrated that the morphological model can be used to derive optimal supersaturation and temperature profiles for a given objective function related to particle shape. Since tracking a supersaturation or temperature profile can be easily achieved via a standard feedback or cascade control system using jacket cooling water, it provides a closed-loop methodology for crystal shape tailoring, which can be easily implemented. Work is underway to investigate an alternative means for manipulating faceted crystal growth by adding impurities.

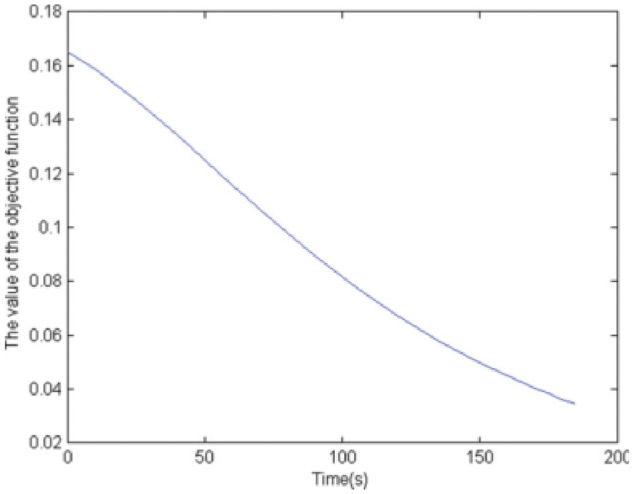

Figure 11. The value of $(x_1/x_2-1)^2 + (x_2/x_3-1)^2$ for the crystal of Figure 10 approaches to zero with time indicating that it grows toward the desired shape.

[Color figure can be viewed in the online issue, which is available at www.interscience.wiley.com.]

Acknowledgments

Financial support from the UK Engineering and Physical Sciences Research Council (EPSRC) for the projects of *Shape* (EP/C009541) and *StereoVision* (EP/E045707) are acknowledged. We would also like to thank the industrial collaborators for the projects including AstraZeneca (Dr. Gerry Steele and Dr. Mike J. Quayle), Malvern Instruments (Mr. Fraiser-McNeil Watron, Dr. Jason Corbett, Mr. David Watson and Mr. Duncan Roberts), Nexia Solutions (Dr. Dominic Rhodes), Pfizer (Dr. Ivan Marziano and Prof. Robert Docherty), Syngenta (Dr. Neil George) and 3M Health Care (Dr. Chris Blatchford). Additional gratitude is also owed to Dr. Rudiyanto Gunawan for the help concerning the software ParticleSolver Version 2.0. The authors are also very grateful for the software Multi-Parametric Toolbox (MPT) by M. Kvasnica, P. Grieder and M. Baotic, which is widely used for the simulation of the article.

Notation

$\boldsymbol{H}$ = matrix
$\boldsymbol{p}$ = vector
m, n, d, z, s, i = scalar
x_1, x_2, x_3 = characteristic parameters of a crystal, μm
r °C/min = cooling rate

$\psi, \Phi, \Psi, \varphi, \Gamma, \phi$ = number population density function, [nb] $\cdot$ m^{-3}
c = solute concentration, mol$\cdot m^{-3}$
c^* = solubility, mol$\cdot m^{-3}$
t = time, s
T = solution temperature, K
σ = relative supersaturation ($= c/c^* - 1$)

Literature Cited

1. Mettler Toledo Ltd. http://us.mt.com.
2. Messtechnik Schwartz GmbH. http://www.mts-duesseldorf.de.
3. IMIX Vision Support Systems. http://www.imix.nl.
4. Calderon de Anda J, Wang XZ, Lai X, Roberts KJ, Jennings KH, Wilkinson MJ, Watson D, Roberts D. Real-time product morphology monitoring in crystallization using imaging technique. *AIChE J*. 2005;51:1406–1414.
5. Wang XZ, Roberts KJ, Ma CY. Crystal growth measurement using 2D and 3D imaging and the perspectives for shape control. *Chem Eng Sci*. 2008;63:1173–1184.
6. Wilkinson MJ, Jennings KH, Hardy M. Non-invasive video imaging for interrogating pharmaceutical crystallization processes. *Microsc Microanal*. 2000;6:996–997.
7. Scott DM, Boxman A, Jochen CE. In-Line Particle Characterization. *Part Part Syst Char*. 1998;15:47–50.
8. Barrett P, Glennon B. Characterizing the metastable zone width and solubility curve using lasentec FBRM and PVM. *Chem Eng Res Des*. 2002;80:799–805.
9. Patience DB, Rawlings JB. Particle-shape monitoring and control in crystallization processes. *AIChE J*. 2001;47:2125–2130.
10. Larsen PA, Rawlings JB, Ferrier NJ. An algorithm for analyzing noisy, in situ images of high-aspect-ratio crystals to monitor particle size distribution. *Chem Eng Sci*. 2006;61:5236–5248.
11. Larsen PA, Rawlings JB, Ferrier NJ. Model-based object recognition to measure crystal size and shape distributions from in situ video images. *Chem Eng Sci*. 2007;62:1430–1441.
12. Qu HY, Louhi-Kultanen M, Kallas J. In-line image analysis on the effects of additives in batch cooling crystallization. *J Cryst Growth*. 2006;289:286–294.
13. Scholl J, Bonalumi D, Vicum L, Mazzotti M, Muller M. In situ monitoring and modeling of the solvent-mediated polymorphic transformation of L-glutamic acid. *Cryst Growth Des*. 2006;6:881–891.
14. Zhou Y, Doan XT, Srinivasan R. Real-time imaging and product quality characterization for control of particulate processes. Marquardt W, Pantelides C. eds. *Joint 16th ESCAPE and 9th PSE: Computer-Aided Chemical Engineering*, *Vol. 21A*, *Garmisch-Partenkirchen*, *Germany*; 2006:775–780.
15. Calderon de Anda J, Wang XZ, Roberts KJ. Multi-scale segmentation image analysis for the in-process monitoring of particle shape with batch crystallisers. *Chem Eng Sci*. 2005;60: 1053–1065.
16. Wan J, Ma CY, Wang XZ. A method for analyzing on-line video images of crystallization at high-solid concentrations. *Particuology*. 2008;6:9–15.
17. Calderon De Anda J, Wang XZ, Lai X, Roberts KJ. Classifying organic crystals via in-process image analysis and the use of monitoring charts to follow polymorphic and morphological changes. *J Process Control*. 2005;15:785–797.
18. Wang XZ, Calderon De Anda J, Roberts KJ. Real-time measurement of the growth rates of individual crystal facets using imaging and image analysis: a feasibility study on needle-shaped crystals of L-glutamic acid. *Chem Eng Res Des*. 2007;85A:921–927.
19. Li RF, Thomson GB, White G, Wang XZ, Anda JCD, Roberts KJ. Integration of crystal morphology modeling and on-line shape measurement. *AIChE J*. 2006;52:2297–2305.
20. Garside J. Industrial crystallization from solution. *Chem Eng Sci*. 1985;40:3–26.
21. Franck R, David R, Villermaux J, Klein JP. Crystallization and precipitation engineering.2. A chemical-reaction engineering approach to salicylic-acid precipitation - Modeling of batch kinetics and application to continuous operation. *Chem Eng Sci*. 1988;43:69–77.
22. Marchal P, David R, Klein JP, Villermaux J. Crystallization and precipitation engineering.1. An efficient method for solving population balance in crystallization with agglomeration. *Chem Eng Sci*. 1988;43:59–67.
23. McCoy BJ. A new population balance model for crystal size distributions: reversible, size-dependent growth and dissolution. *J Colloid Interface Sci*. 2001;240:139–149.
24. Puel F, Fevotte G, Klein JP. Simulation and analysis of industrial crystallization processes through multidimensional population balance equations. Part 1: a resolution algorithm based on the method of classes. *Chem Eng Sci*. 2003;58:3715–3727.
25. Puel F, Fevotte G, Klein JP. Simulation and analysis of industrial crystallization processes through multidimensional population balance equations. Part 2: a study of semi-batch crystallization. *Chem Eng Sci*. 2003;58:3729–3740.
26. Ma DL, Tafti DK, Braatz RD. High-resolution simulation of multidimensional crystal growth. *Ind Eng Chem Res*. 2002;41:6217–6223.
27. Ma DL, Tafti DK, Braatz RD. Optimal control and simulation of multidimensional crystallization processes. *Comput Chem Eng*. 2002;26:1103–1116.
28. Gunawan R, Fusman I, Braatz RD. High resolution algorithms for multidimensional population balance equations. *AIChE J*. 2004;50: 2738–2749.
29. Shi D, El-Farra NH, Li M, Mhaskar P, Christofides PD. Predictive control of particle size distribution in particulate processes. *Chem Eng Sci*. 2006;61:268–281.
30. Ma CY, Wang XZ, Roberts KJ. Morphological population balance for modeling crystal growth in face directions. *AIChE J*. 2008;54: 209–222.
31. Ma CY, Wang XZ. Crystal growth rate dispersion modeling using morphological population balance. *AIChE J*. 2008;54:2321–2334.
32. Zhang Y, Sizemore JP, Doherty MF. Shape evolution of 3-dimensional faceted crystals. *AIChE J*. 2006;52:1906–1915.
33. Snyder RC, Doherty MF. Faceted crystal shape evolution during dissolution or growth. *AIChE J*. 2007;53:1337–1348.
34. Snyder RC, Studener S, Doherty MF. Manipulation of crystal shape by cycles of growth and dissolution. *AIChE J*. 2007;53:1510–1517.
35. Zhang Y, Doherty MF. Simultaneous prediction of crystal shape and size for solution crystallization. *AIChE J*. 2004;50:2101–2112.
36. Gadewar SB, Doherty MF. A dynamic model for evolution of crystal shape. *J Crystal Growth*. 2004;267:239–250.
37. Yu ZQ, Chew JW, Chow PS, Tan RBH. Recent advances in crystallization control - An industrial perspective. *Chem Eng Res Des*. 2007;85:893–905.
38. Lee K, Lee JH, Fujiwara M, Ma DL, Braatz RD. Run-to-Run Control of Multidimensional Crystal Size Distribution in a Batch Crystallizer. *Proceedings of the American Control Conference;* 2002:1013–1018.
39. Yang G, Kubota N, Sha Z, Louhi-Kultanen M, Wang J. Crystal shape control by manipulating supersaturation in batch cooling crystallization. *Cryst Growth Des*. 2006;6:2799–2803.
40. Eiselt HA, Sandblom C-L. A computational study of redundancy in randomly generated polytopes. *Computing*. 1993;49:315–327.
41. Klapper H, Becker RA, Schmiemann D, Faber A. Growth-sector boundaries and growth-rate dispersion in potassium alum crystals. *Cryst Res Technol*. 2002;37:747–757.
42. Ristic RI, Shekunov B, Sherwood JN. Long and short period growth rate variations in potash alum crystals. *J Cryst Growth*. 1996;160:330–336.
43. Ristic RI, Shekunov BY, Sherwood JN. The influence of synchrotron radiation-induced strain on the growth and dissolution of brittle and ductile materials. *J Cryst Growth*. 1997; 179:205–212.
44. Kvasnica M, Grieder P, Baotic M. Multi-Parametric Toolbox (MPT) (http://control.ee.ethz.ch/~mpt/). Cited in 2008.
45. Amara N, Ratsimba B, Wilhelm A, Delmas H. Growth rate of potash alum crystals: comparison of silent and ultrasonic conditions. *Ultrason Sonochem*. 2004;11:17–21.
46. Hulburt HM, Katz S. Some problems in particle technology: A statistical mechanical formulation. *Chem Eng Sci*. 1964;19:555–574.
47. Ramkrishna D, Mahoney AW. Population balance modeling: Promise for the future. *Chem Eng Sci*. 2002;57:595–606.

48. Matsuoka M. Morphology control in melt crystallization. *J Phys D: Appl Phys*. 1993;26:B149–B155.
49. Prywer J. Three-dimensional model of faces disappearance in crystal habit. *J Cryst Growth*. 1995;155:254–259.
50. Prywer J. Kinetic and geometric determination of the growth morphology of bulk crystals: Recent developments. *Prog Cryst Growth Charact Mater*. 2005;50:1–38.
51. Leveque RJ. *Finite volume methods for hyperbolic problems*. Cambridge University Press; 2002.
52. Qamar S, Elsner MP, Angelov IA, Warnecke G, Seidel-Morgenstern A. A comparative study of high resolution schemes for solving population balances in crystallization. *Comput Chem Eng*. 2006;30: 1119–1131.
53. Shi D, Mhaskar P, El-Farra NH, Christofides PD. Predictive control of crystal size distribution in protein crystallization. *Nanotechnol*. 2005;16:S562–S574.
54. Nollet S, Hilgers C, Urai JL. Experimental study of polycrystal growth from an advecting supersaturated fluid in a model fracture. *Geofluids*. 2006;6:185–200.
55. Wan J, Wang XZ, Ma CY. *Model-based optimisation and closed-loop control of crystal shape in cooling crystallisation*. Jezowski J,Thullie J. eds. 19th ESCAPE: *Computer-Aided Chemical Engineering*, Vol. 26, Kracow, Poland; 2009:483–488.
56. Borchert C, Ramkrishna D, Sundmacher K. *Model based prediction of crystal shape distributions*. Jezowski J, Thullie J. eds. 19th ESCAPE: *Computer-Aided Chemical Engineering*, Vol. 26, Kracow, Poland; 2009:141–146.

Manuscript received Aug. 23, 2008, revision received Jan. 13, 2009, and final revision received Mar. 3, 2009.